ACS OMEGA

http://pubs.acs.org/journal/acsodf

Article

Erbium-Doped Nanoparticle–Polymer Composite Thin Films for Photonic Applications: Structural and Optical Properties

Eric Kumi Barimah,* Sri Rahayu, Marcin W. Ziarko, Nikolaos Bamiedakis, Ian H. White, Richard V. Penty, Girish M. Kale, and Gin Jose

Cite This: *ACS Omega* 2020, 5, 9224–9232

Read Online

ACCESS | Metrics & More | Article Recommendations

ABSTRACT: Erbium-doped nanocrystal (NC)-dispersed polymer thin films are attractive core materials for use in optical waveguides as they can provide high optical gain and enable the formation of compact waveguide amplifiers. Nonetheless, there are significant challenges associated with obtaining good dispersibility of NCs into a polymer matrix and favorable optical properties. Therefore, in this paper, we report the fabrication of Er^{3+}-doped ceria (EGC) NCs employing the Leeds alginate process (LAP) and their incorporation into a siloxane polymer matrix. The surface morphology and compositional, structural, and optical properties of the fabricated films are evaluated to assess the NC dispersion and their suitability for the waveguide amplifier. The photoluminescence (PL) and lifetime measurements of the NCs–polymer nanocomposite thin film samples show intense, broadband PL emission of the Er^{3+} ions at 1534 nm ($^4I_{13/2} \rightarrow {}^4I_{15/3}$ transition) with a full width at half-maximum (fwhm) of ∼64 nm and lifetime in the range of 2.6–3.0 ms. The inhomogeneously broadened PL spectra and improvement in lifetime of NCs in the polymer are important results that we report. The EGC NCs–polymer nanocomposite thin films also exhibit excellent transparency in the NIR wavelength range and a refractive index in the range of 1.53–1.58 in the visible wavelength. The work presented here clearly demonstrates the potential of using high-quality Er-doped nanocomposite polymer thin films for interesting applications such as compact low-cost waveguide amplifiers and lasers.

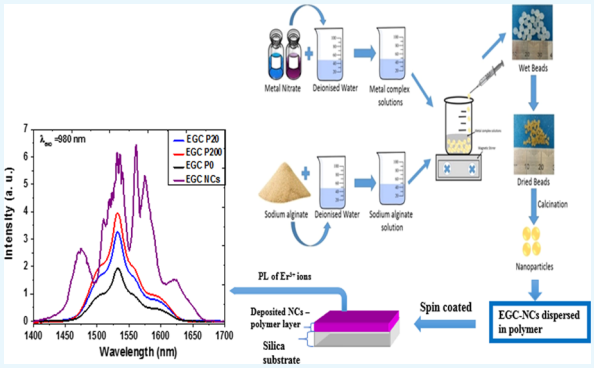

INTRODUCTION

Over the past decade, various polymer materials such as siloxanes, PVA-TEOS, polyimides, polycarbonates, and polyethers have been developed for optical waveguiding and sensing applications. Siloxane materials, in particular, are promising candidates for the formation of low-cost optical waveguides as they possess favorable optical and mechanical properties including high transparency in the visible and NIR range, high thermal stability up to 300 °C, and ease of fabrication.[1] As a result, siloxane-based optical waveguides are currently used for the formation of electro-optical printed circuit boards (EO PCBs) and short-reach flexible optical interconnects.[2−9] However, all such polymer-based optical waveguide circuits are currently purely passive, which limits their use. Although some demonstrations of rare-earth doping in polymer waveguides have been reported,[10,11] no practical integration of active ions in such polymer systems has been achieved yet. As a result, current research targets the formation of low-cost compact waveguide amplifiers that could be used in short-reach optical links.[12]

A practical way to achieve this is by dispersing Er^{3+}-doped nanoparticles (NPs) into the polymer matrix. However, there are a number of important challenges associated with this, as inorganic materials are generally less dispersible in polymers because of particle agglomeration. The dispersion of NPs can be enhanced by having smaller particle sizes, which lead to a high surface area-to-volume ratio for the NPs and therefore yield reduced Rayleigh scattering in the nanocomposite films.[10,11] Good dispersibility of Er^{3+}-doped NPs into polymers can enhance photoluminescence (PL) emission and result in long lifetime at 1534 nm wavelength by suppressing non-radiative processes ascribed to oxygen–hydrogen (O–H) and carbon–hydrogen (C–H) absorption vibrational bands. This is also an important requirement for obtaining high optical gain from such Er^{3+}-doped NPs–polymer nanocomposite optical waveguide amplifiers. Several attempts to achieve efficient dispersion of Er^{3+}-doped NPs in polymer matrices

Received: January 3, 2020
Accepted: March 17, 2020
Published: April 14, 2020

have been reported, and promising results have been achieved.[13,14] Recently, Zhai et al.[13] fabricated $NaYF_4$:Er^{3+}, Yb^{3+}, Ce^{3+} nanocrystals (NCs) and demonstrated a drastic increase in the Er^{3+} ion PL intensity at $^4I_{13/2} \rightarrow {}^4I_{15/2}$ (1.53 μm) transition under 980 nm excitation. The synthesized $NaYF_4$:Er^{3+}, Yb^{3+}, and Ce^{3+} NCs were dispersed in a polymer matrix to obtain Er^{3+}-doped polymer-based optical waveguide amplifiers (EDPWAs) and demonstrated an increase of ~2 dB in the net optical gain because of the presence of Ce^{3+} NCs. Wang et al.[14] synthesized $NaYF_4$/Er^{3+}, Yb^{3+} NCs and constructed EDPWAs with an optical gain of 7.6 dB at 1540 nm in a 15 mm-long waveguide. Furthermore, a 13 mm-long optical waveguide was fabricated based on a core−shell $NaYF_4$/$NaLuF_4$:Er^{3+}, Yb^{3+} NPs−polymethyl methacrylate covalent linking nanocomposite, achieving an optical gain of 15.1 dB at 1530 nm.[15] Most of the previous research is related to fluoride-based particles, and in this research, we propose the use of oxide NPs based on cerium.

Over the last two decades, cerium oxide (ceria) has been extensively investigated as a host material for luminescent lanthanides for various technological applications such as an upconversion for bioimaging,[16−19] solid-state lasers,[20] three-dimensional displays,[21] and electrical conduction mechanism and reliability characteristics related to devices.[22,23] However, these Er^{3+}-doped NPs with comparable phonon energy (450−485 cm^{-1}) will be of potential for fabricating NP−polymer composite waveguides for optical amplification. In particular, doped ceria NPs exhibit high transparency in the visible and NIR regions and high thermal stability.[19−25] The upconversion characteristics and the optical properties in the NIR region of CeO_2:Er^{3+}, Yb^{3+} inverse opals have been reported in demonstrating a significant decrease in upconversion PL intensity of both green and red, and enhanced PL in the NIR centered at 1.56 μm.[26] We also incorporated gadolinium oxide (Gd_2O_3) in the NPs, as they could increase the low phonon energy to ~600 cm^{-1} and increase solubility of other rare-earth ions in ceria.[27] For example, several techniques have been employed to synthesize ceria NPs, which include hydrothermal synthesis, combustion synthesis, and sol−gel.[28−32] For instance, an environmentally friendly carbon neutral sol−gel method called the leeds alginate process (LAP) has been developed by Kale et al.[18,33] for synthesizing crystalline complex functional ceramic oxide NPs of controlled stoichiometry in a single step.

Therefore, in this work, we prepared the Er^{3+}-doped CeO_2-GdO_2 NPs dispersed in siloxane polymer thin films and studied their PL intensity at 1.5 μm. The fabrication method is compatible with board-level integration, while the produced polymer nanocomposite films show great potential to form high-gain Er^{3+}-doped waveguide amplifiers. The size and morphology of the NCs, the film surface quality, and its optical properties are thoroughly studied. The obtained results demonstrate good surface quality and excellent optical properties, indicating their potential to form low-cost optical sensors and waveguide amplifiers using this technology.

RESULTS AND DISCUSSION

Structure and Morphology of EGC NCs and Polymer Nanocomposite Thin Film. The fabrication of the Er^{3+}-doped ceria (EGC) NCs is based on the LAP sol−gel technique[24] and is described in the Experimental Section of the paper. Figure 1 shows a high-resolution transmission electron microscopy (HR-TEM) image and a selected-area electron-

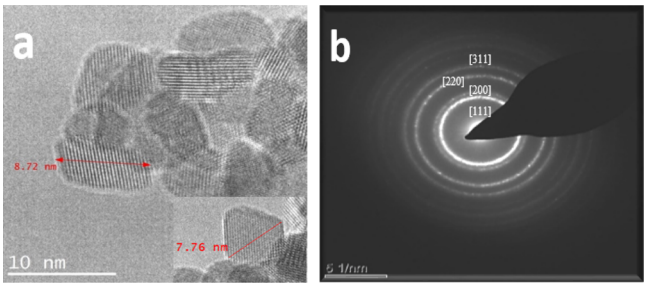

Figure 1. (a) HRTEM image of EGC NCs at 10 nm scale and (b) SAED patterns taken from EGC NCs.

diffraction (SAED) pattern obtained from the synthesized phase pure EGC NCs after 2 h calcination at 500 °C. The structure and morphology observed in Figure 1a show that almost all EGC NCs are agglomerated and that they have a cubic shape. Their size is estimated to be in the range of 7−10 nm. The SAED image of the EGC NCs in Figure 1b suggests that the particles have a uniform fine grain size of polycrystalline and well-defined lattice parameters, as the individual spherical concentric rings around the central spot can be clearly distinguished. The analysis of the SAED pattern [spherical rings in Figure 1b] reveals an interplanar spacing of 0.313, 0.285, 0.192, 0.163, and 0.124 nm, which are indexed as the lattice parameters of the (111), (200), (220), (311), and (222) planes of the cubic crystal systems. The energy-dispersive X-ray (EDX) spectroscopy was used to map the various elements present in the EGC NCs, and the results are shown in Figure 2. It includes the element X-ray maps obtained for erbium (Er), gadolinium (Gd), cerium (Ce), and oxygen (O). The low color density of the Er and Gd maps compared to the Ce image map [Figure 2] reflects variation in the doping concentration. This study confirms the presence of the various elements within the EGC NCs.

The EGC NCs were initially dispersed in toluene solution and then mixed with siloxane polymer to produce a polymer nanocomposite solution (EGC P0). The solution was mixed using magnetic stirring for about 20 min. A part of it was filtered using two Whatman syringe filters (Cat. no. 6809-1002_Anotop 10 mm and Cat. no. 6870-1302 _GD/X 13 mm) of different membrane pore sizes: 0.02 μm (EGC P20) and 0.20 μm (EGC P200), to remove any individual or clusters of EGC NCs with the size larger than the membrane pore size. The two filtered and the unfiltered solutions were used to fabricate three EGC NCs−siloxane nanocomposite thin film samples. Each solution was deposited on a silica substrate using spin coating and was UV-exposed to produce a polymer nanocomposite thin film of average thickness ~10.0 μm. The details of the synthesis of the EGC NCs and the fabrication of the EGC NCs−polymer nanocomposite thin film samples are described in the Experimental Section. A plain (without any EGC NCs) polymer thin film sample (PoS) of similar thickness was also produced on a silica substrate as a reference sample.

Figure 3 shows SEM images of the surface of the fabricated EGC NCs−siloxane nanocomposite thin films. The SEM images obtained from the filtered samples EGC-P20 [Figure 3a] and EGC-P200 [Figure 3b] show good uniformity and even thickness, with no cracks or isolated EGC NCs observed. On the other hand, the unfiltered sample EGC-P0 [Figure 3c] shows strong agglomeration of NCs on the sample surface. The SEM images in Figure 3 were further analyzed with

https://dx.doi.org/10.1021/acsomega.0c00040
ACS Omega 2020, 5, 9224−9232

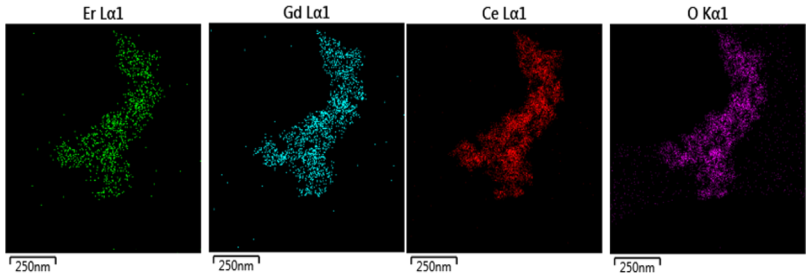

Figure 2. EDX−STEM elemental mapping images from EGC NCs consist of erbium, gadolinium, cerium, and oxygen which are in green, blue, red, and pink colours, respectively.

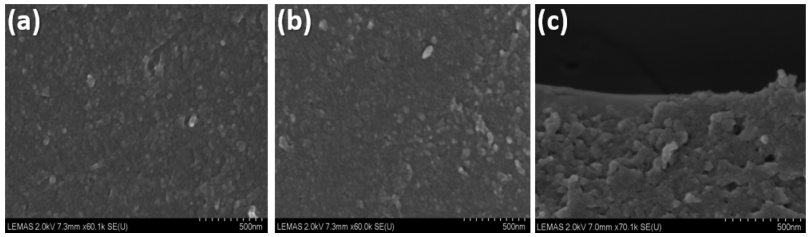

Figure 3. SEM images of hybrid EGC NCs−polymer nanocomposites thin film on silica substrates using (a) EGC-P20, (b) EGC-P200, and (c) EGC-P0.

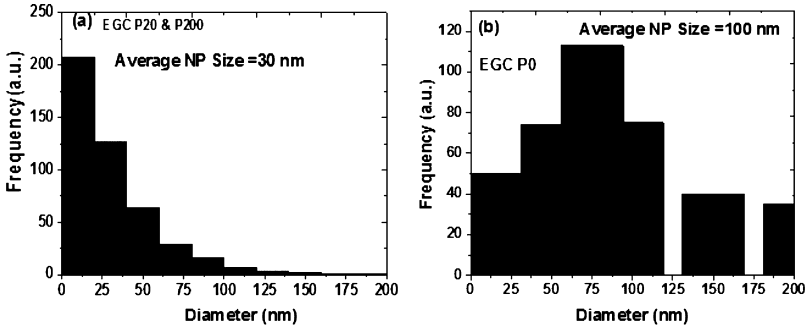

Figure 4. Size distribution histograms of the EGC NCs in the polymer nanocomposite films for the three samples using (a) EGC P20 and P200, and (b) EGC P0.

ImageJ software to determine the size of the NCs dispersed in the siloxane film. Figure 4 shows the obtained histogram of the size distribution of ECG-NCs for the three samples, and the corresponding average size were obtained: ∼30 nm (EGC P20 and EGC P200) and ∼100 nm (EGC-P0). The results demonstrate the importance of the filtering step for the formation of uniform films with small NCs sizes. However, using the ImageJ software findings indicated that the EGC P20 nanocomposite thin film has larger particle size (>20 nm) than expected. Such disagreement in the particle size may be attributed to the polymer encapsulate of the smaller NPs to form larger particles, which was certainly inevitable. The size of the NCs is important in minimizing optical loss due to Rayleigh scattering in such nanocomposite thin films. Simulations based on the Mie theory[34] indicate that NCs with sizes <10 nm result in additional losses of 0.1 dB/cm at 1550 nm wavelength. Chen et al.[35] reported an additional loss of 0.3 dB/cm at 1534 nm for rare-earth-doped $NaYF_4$ NCs, with an average particle size of 22 nm dispersed in SU8. Moreover, sample EGC-P200 has an average NCs size of ∼30 nm which was as expected because of the large membrane pore size of the filter as compared to the membrane pore size of sample EGC-P20.

The samples were prepared for milling using focused ion beam (FIB) to enable the study of their cross-section. About 30 and 500 nm thick iridium and gallium ions were deposited onto the EGC NCs−siloxane polymer nanocomposite layer prior to the milling in order to protect the thin film from damage during the process. Gallium ion beam energy of 30 kV and a current of 0.79 nA were employed for all steps in the milling process, while the final sample polishing was done with a voltage of 5 kV and a current of 41 pA. Figure 5 shows FIB−SEM images of the cross-section of samples EGC P0

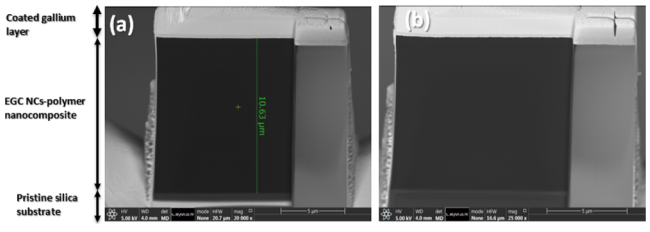

Figure 5. FIB−SEM images of the cross-section of samples (a) EGC P200 and (b) EGC P0 showing a clear contrast between the deposited gallium ion layer, the polymer nanocomposite layer, and the silica substrate.

https://dx.doi.org/10.1021/acsomega.0c00040
ACS Omega 2020, 5, 9224−9232

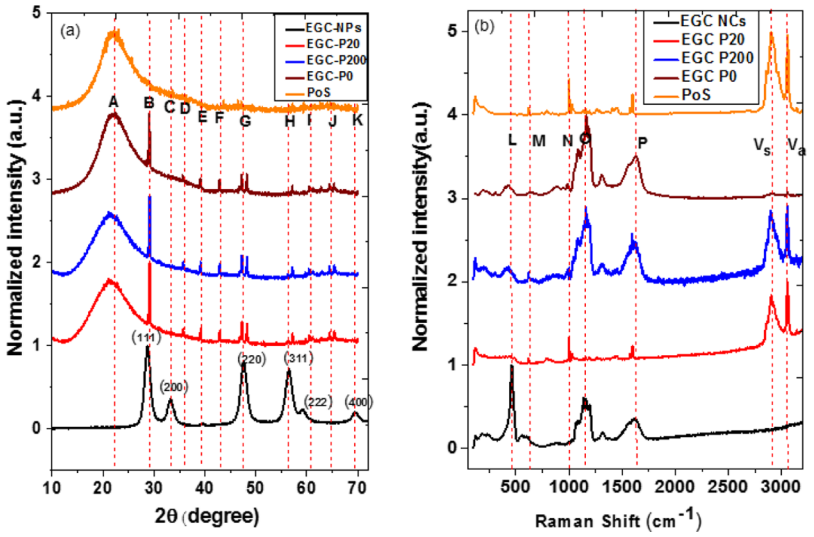

Figure 6. (a) XRD patterns and (b) Raman shift of the EGC-NCs sample calcined at 500 °C for 2 h, polymer on silica substrate (PoS), EGC-NCs, and polymer nanocomposite samples (EGC-P0, EGC-P20, and EGC-P200).

(unfiltered) and EGC P200 (filtered with 0.2 μm pores). The section removed using FIB exhibits a uniform EGC NCs−siloxane polymer layer interface without any obvious NCs clusters and shows clear distinction between the gallium layer, the polymer nanocomposite film with the dark background, and the underlying pristine silica substrate.

The crystal phase identification patterns of the EGC NCs and EGC-NCs−polymer nanocomposite film (EGC-P0, EGC-P20 and EGC-P200) were also acquired using the Philips PANalytical X'pert diffractometer with Cu Kα radiation at 40 kV and 40 mA. Figure 6a shows the X-ray diffraction (XRD) patterns obtained from the plain EGC NCs (as-synthesized) and the nanocomposite polymer samples. The diffraction patterns of EGC NPs are quite intense and broad with peak intensities centered at 2θ = 28.43° (peak B), 33.06° (peak C), 47.28° (peak G), 56.09° (peak H), 59.05° (peak I), and 69.36° (peak K), which correspond to the (111), (200), (220), (311), (222), and (400) planes of the cubic fluorite structure of CeO_2. The relative intensities correlate well with the ICDD number 04-012-3419 literature value or with the ICDD 98-015-5604 pattern and space group of $Fm\bar{3}m$. These crystal phases are identified as cerium gadolinium oxide ($Ce_{0.8}Gd_{0.2}O_{1.9}$) from the EGC NCs. In addition, new crystalline structures appear in the diffraction patterns of all three fabricated EGC NCs−siloxane polymer nanocomposite thin films. The presence of sharp diffraction patterns from the polymer nanocomposite thin films indicates the low ratio of surface to volume atom and improved crystal dispersion, which was not observed in the pure EGC NCs. It is possible that the EGC NCs atoms are not fully coordinated or EGC NCs atoms are covered by the polymer, and therefore can alter the lattice parameter of the unit cell. This can distort the XRD pattern spectrum. The peaks located at 2θ = 35.79° (peak E), 42.98° (peak F), 47.31° (split peaks G), and 64.50° (split peaks J) can be attributed to the (411), (134), (440), and (622) planes and indexed as a cubic crystal structure (ICDD: 04-011-5933 with the space group of $Ia\bar{3}$). These peaks were not present in the EGC NCs diffraction patterns. Further analysis reveals that the new crystalline phase formation produces peaks at a diffraction angle of 2θ = 47.31° (440), 48.32° (440), and 57.68° (622), which could be ascribed to the erbium gadolinium oxide ($Er_{1.6}Gd_{0.4}O_3$) cubic structure (ICDD no. 04-019-6501). The existence of these peaks can be attributed to the excellent dispersion of the NCs in the polymer host. As shown in Figure 6a, the diffraction pattern of both plain and nanocomposite siloxane polymer thin films exhibits a broad peak centered at 2θ = 23.5° (peak A), which represents a short-range structure of the amorphous silica substrate.[36]

Furthermore, the average crystallite size, (D_{khl}), of the pure EGC NCs and its polymer nanocomposite thin films was estimated using the X-ray diffraction patterns and well-known Scherrer's formula, which is expressed as[37]

$$D_{khl} = \frac{K\lambda}{\beta \cos(\theta)}$$

where λ is the X-ray wavelength (0.15405 nm), β is the full width at half width at full-maximum of the diffraction peak, and K is a constant related to the crystallite shape (0.94). The diffraction peaks centered at 2θ = 29.11 and 47.21 were used to calculate the average crystallite size, which was obtained to be ∼8, 23, 26, and 76 nm for EGC NCs, EGC-P20, EGC-P200, and EGC-P0, respectively. The average crystallite sizes obtained show good agreement with the particle sizes observed in the TEM and SEM measurements (Figures 1 and 2).

The Raman spectra were also recorded with a Renishaw Raman spectrometer using a laser excitation wavelength of 514.5 nm. Figure 6b shows the different vibrational spectra obtained from the polymer thin film without EGC NCs, EGC NCs, and the polymer film with EGC-NCs. The Raman spectrum of the EGC NCs exhibits a sharp band of ceria at 465 cm^{-1} (peak L),[38] which can be ascribed to the Ce−O Raman-active vibrational band (F_{2g}) of the fluorite-type structure. In addition to this, the Raman spectrum of the EGC NCs reveals a weak band range from 500 to 650 cm^{-1} with a peak at 560 cm^{-1}, which can be associated with oxygen vacancies defects induced by the Er^{3+} and Gd^{3+} ion substitution in CeO_2 upon doping. Such distortions in the ceria coordination environment can occur from intrinsic defects because of the elevated temperatures during sintering and the high concentration of Er^{3+} and Gd^{3+} ions.[27] Similar observations have been found in the literature. For instance, Florea et al.[19] demonstrated an enhancement in the oxygen vacancies defects band centered at

https://dx.doi.org/10.1021/acsomega.0c00040
ACS Omega 2020, 5, 9224−9232

550 cm^{-1} with increasing La^{3+} ion concentration in doped Er–CeO_2. Their work showed that the 550 cm^{-1} Raman spectrum band broadened and shifted to lower frequencies, as the La^{3+} ion concentration increased. Similarly, Porosmicu et al.[25] analyzed different concentrations of (0.3, 1, 3%) Er^{3+} ion-doped CeO_2 and 1% Er, 20% Yb-codoped CeO_2 and demonstrated similar behavior with a significant enhancement of the defect's spectrum band around 550 cm^{-1}. The band peaks around 1127 cm^{-1} (peak O) and 1600 cm^{-1} (peak P) result from the Er^{3+} PL fluorescence of $^2H_{11/2}$–$^4I_{15/2}$ (547 nm) and $^4S_{3/2}$–$^4I_{15/2}$ (560 nm) transitions, respectively.[36,39] However, the two PL emission peaks (O and P) could not be detected in the filtered EGC P20 sample. This can be attributed to the low concentration of the EGC NCs, the small particle size, and the encapsulation of the EGC NCs using the polymer after microfiltration. It is important to mention that the oxygen vacancy defect peak at 560 cm^{-1} observed in EGC NCs Raman spectrum (Figure 6b) has shifted to 654 cm^{-1} for sample EGC P0, and it is not observed at all in EGC P20 and EGC P200 samples. Furthermore, the Raman spectrum of the undoped polymer thin film (polymer-on-silica) exhibits various peaks centered at ∼623 cm^{-1} (peak M), 1026 cm^{-1} (peak N), 1600 cm^{-1} (peak P), 2900 cm^{-1} (peak V_s), and 3050 cm^{-1} (peak V_a), which have also been reported previously.[36] The strong bands at 2900 cm^{-1} (peak V_s) and 3050 cm^{-1} (peak V_a) are observed in all polymer nanocomposite thin films and can be ascribed to CH_3 symmetric and asymmetric stretching vibrations.[40,41] The band at 623 cm^{-1} is attributed to Si–C symmetric stretching, while those centered at 1023 and 1600 cm^{-1} can be attributed to symmetric and asymmetric vibrational modes of CH_3. The weak broad Raman vibrational band range from 100 to 250 cm^{-1} corresponds to SiC_3 symmetrical mode deformation.[40,41] As expected, the weak broad band of the ceria Raman-active mode at 461 cm^{-1} is detected in all the polymer nanocomposite samples. It is important to mention that the signal strength of the ceria Raman-active mode of the polymer nanocomposite films depends on the concentration of EGC NCs and the particle size embedded in the polymer.

Optical Properties of EGC NCs and Polymer Nanocomposite Thin Film. Figure 7 shows the PL upconversion emission spectra of the EGC NCs and the three different EGC NCs–siloxane polymer nanocomposite thin films under 980 nm excitation. The three upconversion peaks centered at 548, 562, and 668 nm observed in the plain EGC NCs and the unfiltered EGC P0 sample correspond to the $^2H_{11/2}$–$^4I_{15/2}$, $^4S_{3/2}$–$^4I_{15/2}$, and $^4F_{9/2}$–$^4I_{15/2}$ 4f-intraband transitions of the Er^{3+} ions. The PL intensity in the green band relative to red emission band for sample EGC P0 is enhanced as compared the plain EGC NCs. However, the intensity of green emission of the filtered samples EGC P20 and EGC P200 is substantially lower. In contrast, the red emission band of these two samples disappears completely. Significant reduction of upconversion peaks can be ascribed to the photo-assisted energy transfer from Er^{3+}($^2H_{11/2}$) to Ce^{3+}($^2F_{7/2}$) levels as larger clusters are removed. Furthermore, PL lifetime measurements were conducted to characterize the EGC NCs–polymer nanocomposite thin films in the visible range. The lifetimes obtained at 543/548, 562, and 668 nm for the EGC NCs and thin film samples are reported in Table 1. The PL lifetime values of the plain EGC NCs at the different upconversion peak wavelengths are found to be larger than those of the EGC NCs–polymer nanocomposite films, which is attributed to the nonradiative relaxation of EGC NCs in the polymer matrix. This suggests that the PL emission of larger size EGC NCs is more efficient with less nonradiative decay effects, as the dopants within the crystals are less affected by polymer ligands with higher phonon energies.

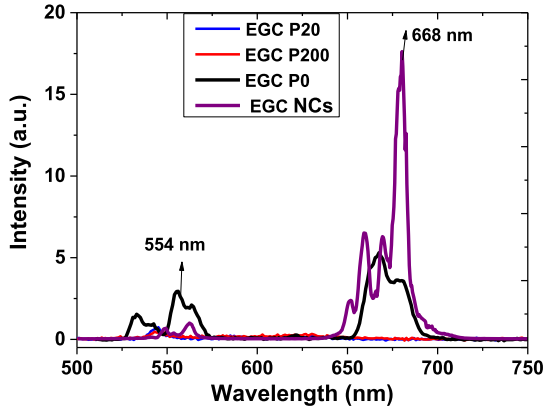

Figure 7. PL upconversion spectrum of the pure EGC NCs and three nanocomposite samples.

Table 1. Bandwidth and an Average Lifetime of EGC NPs, Hybrid of EGC NCs–Siloxane Polymer (EGC P0), and Filtered Samples (EGC P20 and EGC P200)

sample name	lifetime at 543/554 nm (μs)	lifetime at 680 nm (μs)	$\Delta\lambda_{eff}$ at 1534 nm (nm)	lifetime at 1534 nm (ms)
EGC P20	17		63.95	2.95
EGC P200	11		63.64	2.73
EGC P0	18	9	63.57	2.63
EGC NCs	96	239	88.70	2.14

Figure 8a shows the room-temperature PL spectrum obtained from the as-synthesized nanocrystals (EGC NCs) and the three nanocomposite polymer samples upon excitation with a 980 nm laser. A broad and intense PL spectrum is observed at 1534 nm, which is assigned to the Er^{3+} ion $^4I_{13/2} \rightarrow {}^4I_{15/3}$ transition of the EGC NCs. In addition, the PL spectrum of the pure EGC NCs reveals four additional overlapping sharp emission peaks located at 1476, 1561, 1576, and 1622 nm, which are attributed to the stark splitting effect.[42] The stark splitting occurs because of the local electric-field induced by the crystal field around the Er^{3+} ions in the Gd^{3+}-doped CeO_2 NCs matrix.[43,44] As can be seen in Figure 8a, the shape of the PL spectrum of the three nanocomposite thin film samples is identical with its peak intensity centered at 1534 nm, as compared to the EGC NCs. The PL spectrum of the polymer nanocomposite looks similar to that obtained from the Er^{3+} ion-doped glass or glass ceramics matrix.[45,46] This is exciting as it is a direct evidence that the Er^{3+} ions are distributed sites that contribute to all transitions between the Stark-splitted $^4I_{13/2}$ and $^4I_{15/2}$ levels. Consequently, we observed an inhomogeneously broadened spectrum in the C-band of optical communication suitable for engineering planar waveguide amplifier with this composite material. Further investigation is conducted to determine the most efficient

https://dx.doi.org/10.1021/acsomega.0c00040
ACS Omega 2020, 5, 9224–9232

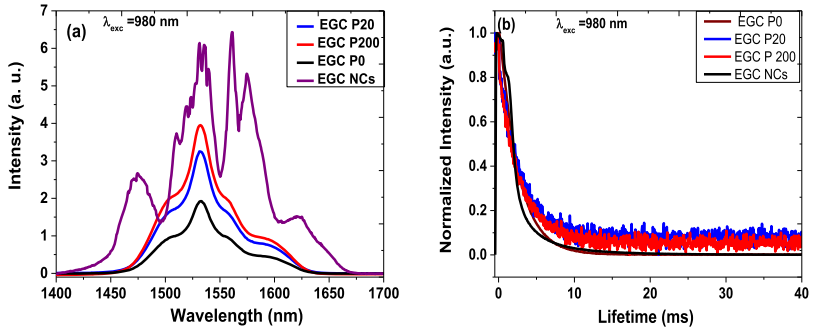

Figure 8. (a) NIR PL spectrum and (b) PL lifetime of the pure EGC NCs and three nanocomposite samples.

membrane filter pore size required for the filtering of the EGC NCs. Comparison of the PL intensity obtained from the filtered samples (EGC P20 and EGC P200) with that from the unfiltered sample (EGC P0) shows an increase in PL intensity by a factor of ∼1.7 and 2.0, respectively. The increase in the broad emission peak at 1534 nm could be ascribed to the lack of cooperative upconversion from the Er^{3+} excitation ($^4I_{11/2}$) and emission ($^4I_{13/2}$) levels because of the increase in the ion−ion distance, as discussed before in the context of the upconversion process. On the other hand, the enhanced PL intensity at $^4I_{13/2} \rightarrow {}^4I_{13/2}$ transition of Er^{3+} ion can be ascribed to the cross-relaxation energy transfer between Er^{3+} and C^{3+}. The excited Er^{3+} ions undergo energy transfer from its $^4I_{11/2}$ state to $Ce^{3+}(^2F_{7/2})$ state and then returns to the $^4I_{13/2}$ state of the Er^{3+} ion at a fast rate.[47] Thus, the PL intensity and broadband at 1534 nm are enhanced owing to increased population of the $^4I_{13/2}$ state from the $Ce^{3+}(^2F_{5/2})$. Furthermore, the enhancement in the polymer nanocomposite PL spectrum with the decreasing membrane filter pore size can be explained by decreasing the EGC NCs concentration dispersed in the polymer, which leads to an increase in the distance between Er^{3+} ions in the host crystal. As a consequence, the non-radiative process is suppressed and the efficiency of the radiative process is enhanced. This is further supported by the PL lifetime measurement (Figure 8b), and the lifetime data are provided in Table 1. The room temperature lifetime of the EGC NCs is found not to be single exponential, while the fabricated nanocomposite samples exhibit an exponential decay at 1534 nm (Figure 8b). The average lifetime, τ_{ave}, for each sample was therefore calculated using the integrated decay curve normalized to the initial intensity for better comparison[48]

$$\tau_{ave} = \frac{\int_0^{t_\alpha} tI(t)\mathrm{d}t}{\int_0^{t_\alpha} I(t)\mathrm{d}t}$$

where $I(t)$ represents the PL intensity at time t.

The $^4I_{13/2}$ state lifetime increased when the average NC particle size in the composite is decreased. This indicates that the dispersed EGC NCs in the polymer do not have any effect on the Er^{3+} ion $^4I1_{3/2}$ state lifetime but rather enhances it.

The fluorescence line width, $\Delta\lambda_{eff}$, of the PL emission spectrum was calculated using the expression[49]

$$\Delta\lambda_{eff} = \frac{\int I(\lambda)\mathrm{d}\lambda}{I_{max}}$$

where $I(\lambda)$ and I_{max} are the measured emission intensity at wavelength λ and peak emission wavelength, respectively.

Table 1 displays the calculated fluorescence line width of the pure EGC NCs and the three nanocomposite samples. The PL spectrum of the pure EGC NCs is centered at 1534 nm and exhibits a fluorescence line width of 88.70 nm, but the fluorescence line width $\Delta\lambda_{eff}$ of samples EGC P0, EGC P20, and EGC P200 are found to be around 63 nm. The large fluorescence line width values obtained for the nanocomposite thin films are comparable to Er^{3+}-doped phosphate glass hosts reported by Jiang et al.,[50] which have been used to fabricate the waveguide amplifier.

The transmittance of the three nanocomposite samples was also investigated over the spectral range 250−1700 nm using a PerkinElmer Lamda 905 UV−visible−NIR spectrometer (Figure 9). The results demonstrate high transmittance of

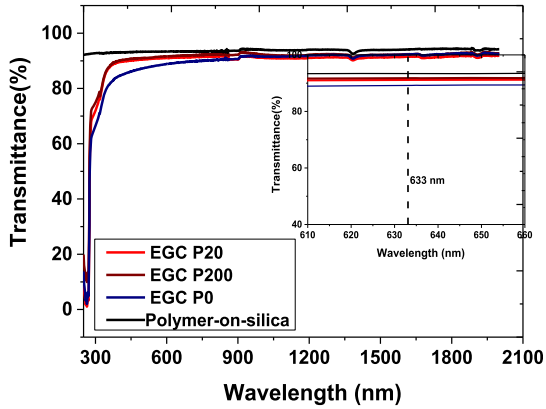

Figure 9. UV−vis−NIR transmission spectra of the silica substrate and hybrid of EGC NPs−siloxane polymer nanocomposite thin films.

about 92% within the spectral range of 720−2000 nm and a strong absorption around 380 nm for all three nanocomposite polymer samples. The transmission dip in the UV is not observed in the plain polymer-on-silica sample (PoS), indicating that this is due to the presence of the EGC NCs. An inset in the Figure 9 shows the comparison of the transmittance at 633 nm, which clearly illustrates that the transmittance at this wavelength for samples EGC P20 and EGC P200 is identical.

The refractive index is an important parameter when designing optical waveguides, so the refractive index of the fabricated EGC NCs−polymer nanocomposite thin films is measured using spectroscopic ellipsometry. The measurements were carried out in the wavelength range 350−900 nm in steps of 5 nm and provide both the real (n) and imaginary part (extinction coefficient k) of the refractive index of the nanocomposite polymer thin films. The real and imaginary

https://dx.doi.org/10.1021/acsomega.0c00040
ACS Omega 2020, 5, 9224−9232

refractive index values of 1.5473 and 0.0096 at 633 nm were obtained for samples EGC P20 and EGC P200, respectively. The refractive index of a plain polymer-on-silica sample (PoS) is also measured for reference using a Metricon prism coupler (model 2010) and was found to be 1.512 at 633 nm. The knowledge of the refractive index values of the substrate and polymer films enables the correct design of waveguides at a particular wavelength.

CONCLUSIONS

The combination of Er-doped ceria NCs and siloxane polymer materials can provide high-quality nanocomposite thin films with good optical properties, which could be used for the formation of cost-effective waveguide amplifiers and optical sensors. Simple fabrication methods are employed to produce the films, while microfiltering is applied to improve the dispersion of the NCs in the polymer matrix. Er^{3+}, Gd^{3+} codoped ceria NCs are prepared using the novel LAP sol–gel technique, and their morphology and optical properties are studied prior to their dispersion in the siloxane materials. TEM analysis reveals that the EGC NCs have a crystallite size range from 7 to 10 nm. The EGC NCs are dispersed in siloxane polymer materials using microfiltration techniques, with the intention of improving the dispersion of EGC NCs in the polymer matrix and minimizing their agglomeration in larger-size clusters. SEM images obtained from the filtered nanocomposite samples show well-dispersed EGC NCs in polymer nanocomposite thin films and high surface quality as compared with the unfiltered EGC NCs–polymer nanocomposite thin film. A broad and intense PL emission spectrum centered at 1534 nm is obtained from the fabricated thin films with a fluorescence line width of ∼64 nm, while the PL lifetime is found to be in the range 2.6–2.9 ms and increase with decreasing EGC NC crystallite size. A significant enhancement of the PL intensity at 1534 nm is obtained from the nanocomposite thin films when filtration is applied. Overall, the characterization of the EGC NCs–siloxane polymer nanocomposite films demonstrates good optical properties and indicates great potential for the formation of EDPWAs, lasers, and sensors.

EXPERIMENTAL SECTION

Manufacturing EGC-NCs and Polymer Nanocomposite Thin Films. NPs of $Ce_{0.8}Er_{0.1}Gd_{0.1}O_{1.9}$ were prepared using the process called LAP developed by Kale and co-workers,[18,33] from commercial $Ce(NO_3)_3{\cdot}6H_2O$ (>99% of purity), $Er(NO_3)_3{\cdot}xH_2O$ (>99.9% of purity), and $Gd(NO_3)_3{\cdot}6H_2O$ (>99.9% of purity). The preparation procedure is shown in Figure 10. Two kinds of solutions were prepared under magnetic stirring, then, the sodium alginate solution solution was dripped into the metal complex solution using a 16-gauge stainless-steel needle attached to a syringe. After maintaining the gel beads phase for 14 h, the wet metal-alginate beads were dried at 90 °C for 24 h. The dry beads were calcined at 500 °C for 2 h in an ambient atmosphere to transform from metal beads into NPs. The optimum calcination temperature was determined by performing simultaneous DSC–TGA–DTG experiments on dried beads. About 0.1% volume fraction of the dry powder of the EGC NCs was diluted with toluene as a precursor solution and was mixed with siloxane polymer (Dow Corning Corporation WG-2020 Optical Elastomer) using magnetic stirring for about 20 min to obtain good uniformity

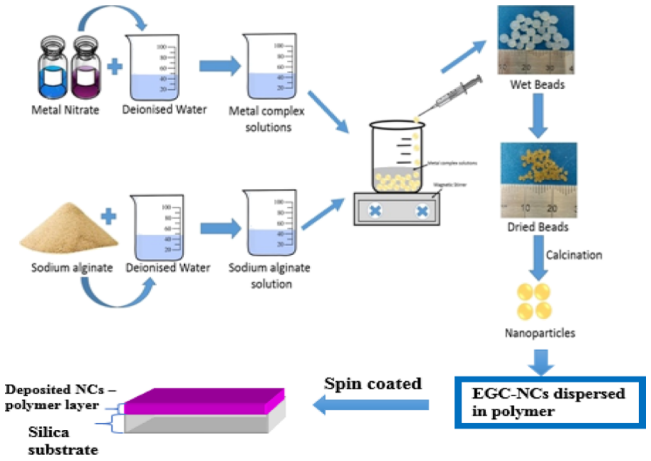

Figure 10. Flow diagram of the LAP for manufacturing EGC NCs and fabrication of EGC NCs–polymer nanocomposite thin film.

and dispersibility. The EGC NCs–siloxane polymer nanocomposite solution was filtered through 0.02 μm (EGC-P20) and 0.20 μm (EGC-P200) membrane pore size syringe filters. Microfiltration was employed to remove large particles with size greater than the membrane pore size. Three different nanocomposite solutions were prepared: one unfiltered (EGC-P0) and two filtered (EGC-P20, and EGC-P200) and were used to produce thin film samples. Each EGC NCs–polymer nanocomposite solution was spin-coated onto the 30 mm × 20 mm silica substrate at 1000 rpm revolution speed for 1 min, followed by UV exposure and a baking step (100 °C for 5 min) to produce a planar nanocomposite thin film.

Structural and Optical Characterization. The NC size and morphology were examined under a HRTEM (FEI Tecnai TF20 operated at 200 kV fitted with a Gatan Orius CCD camera and Oxford instruments 80 mm^2). The EGC NCs were dispersed in deionized water, and a drop of the solution was taken onto carbon-coated copper grids and allowed to dry in a vacuum oven for TEM analysis. The surface morphology of the EGC NCs–polymer composite thin films was characterized using a high-resolution field emission gun scanning electron microscope (FEGSEM) with precise FIB (FEI Helios G4 CX DualBeam). The element identification, cross-sectional compositional contrast of the different atomic numbers, and their distribution in the NCs and thin films were measured by scanning (S)/TEM EDX spectroscopy imaging. XRD analysis of EGC NCs and EGC NCs–polymer nanocomposite thin films were performed using a Philips PANalytical X'pert diffractometer with Cu Kα radiation (λ = 1.54056 Å) at 40 kV and 100 mA. The XRD patterns were recorded from 10 to 70° with a step size of 0.02 for angle 2θ. HighScore data analysis was utilized to analyze the retrieved structural refinement from the XRD data. Raman measurements were also carried out to investigate the structural arrangement of the NPs and the EGC NPs–polymer composite thin films using a Renishaw in via Raman spectrometer with a green Ar^+ laser (λ = 514.5 nm) excitation source. The FS920 spectrometer (Edinburgh Instruments, UK) and semiconductor laser diode with the excitation wavelength of 980 nm was employed to measure downconversion PL and lifetime of the NCs and EGC NCs–polymer composite films at room temperature. The optical transmission of the thin film was recorded using a PerkinElmer Lambda 905 UV–visible–NIR spectrometer, while the

https://dx.doi.org/10.1021/acsomega.0c00040
ACS Omega 2020, 5, 9224–9232

refractive indices were measured by ellipsometry (Woollam M-2000XI).

AUTHOR INFORMATION

Corresponding Author

Eric Kumi Barimah − *School of Chemical and Process Engineering, University of Leeds, Leeds LS2 9JT, U.K.*; orcid.org/0000-0003-4841-9866; Email: e.kumi-barimah@leeds.ac.uk

Authors

Sri Rahayu − *School of Chemical and Process Engineering, University of Leeds, Leeds LS2 9JT, U.K.*

Marcin W. Ziarko − *Centre for Photonic Systems, Department of Engineering, University of Cambridge, Cambridge CB3 0FA, U.K.*

Nikolaos Bamiedakis − *Centre for Photonic Systems, Department of Engineering, University of Cambridge, Cambridge CB3 0FA, U.K.*

Ian H. White − *Centre for Photonic Systems, Department of Engineering, University of Cambridge, Cambridge CB3 0FA, U.K.; University of Bath, Bath BA2 7AY, U.K.*

Richard V. Penty − *Centre for Photonic Systems, Department of Engineering, University of Cambridge, Cambridge CB3 0FA, U.K.*

Girish M. Kale − *School of Chemical and Process Engineering, University of Leeds, Leeds LS2 9JT, U.K.*; orcid.org/0000-0002-3021-5905

Gin Jose − *School of Chemical and Process Engineering, University of Leeds, Leeds LS2 9JT, U.K.*

Complete contact information is available at: https://pubs.acs.org/10.1021/acsomega.0c00040

Notes

The authors declare no competing financial interest.

ACKNOWLEDGMENTS

This work was supported by Engineering and Physical Science Research Council (EPSRC) financial support through the SeaMatics research grant (EP/M015165/1) and Dow Corning for the provision of the polymer materials. The second author is grateful for the financial support from Ministry of Research, Technology and Higher Education of the Republic of Indonesia for a scholarship through Riset-Pro (Loan number 8245-ID). The authors thank Dr. Zabeada Aslam and Mr. John Harrington, Leeds Electron Microscopy and Spectroscopy (LEMAS) Centre, for support in carrying out the TEM and FIB measurements.

REFERENCES

(1) Molina, C.; Moreira, P. J.; Gonçalves, R. R.; Sá Ferreira, R. A.; Messaddeq, Y.; Ribeiro, S. J. L.; Soppera, O.; Leite, A. P.; Marques, P. V. S.; de Zea Bermudez, V.; Carlos, L. D. Planar and UV written channel optical waveguides prepared with siloxane−poly(oxyethylene)−zirconia organic−inorganic hybrids. Structure and optical properties. *J. Mater. Chem.* **2005**, *15*, 3937−3945.

(2) Selviah, D. R. Polymer Multimode Waveguide Optical and Electronic PCB Manufacturing, Proc. SPIE 7219, *Optoelectronic Integrated Circuits XI*, 2009; 721905.

(3) Neyer, A.; Kopetz, S.; Rabe, E.; Kang, W. J.; Tombrink, S. Electrical-Optical Circuit Board Using Polysiloxane Optical Waveguide Layer. *Proceedings Electronic Components and Technology*, 2005; pp 246−250.

(4) Cai, D.; Neyer, A. Design for reliability of polysiloxane-based electrical-optical circuit boards. *Appl. Opt.* **2010**, *49*, 4113−4119.

(5) Bamiedakis, N.; Hashim, A.; Penty, R. V.; White, I. H. A 40 Gb/s Optical Bus for Optical Backplane Interconnections. *J. Lightwave Technol.* **2014**, *32*, 1526−1537.

(6) Bamiedakis, N.; Hashim, A.; Beals, J.; Penty, R. V.; White, I. Low-Cost PCB-Integrated 10-Gb/s Optical Transceiver Built with a Novel Integration Method. *IEEE Trans. Compon., Packag., Manuf. Technol.* **2013**, *3*, 592−600.

(7) Dangel, R.; Horst, F.; Jubin, D.; Meier, N.; Weiss, J.; Offrein, B. J.; Swatowski, B. W.; Amb, C. M.; DeShazer, D. J.; Weidner, W. K. Development of Versatile Polymer Waveguide Flex Technology for Use in Optical Interconnects. *J. Lightwave Technol.* **2013**, *31*, 3915−3926.

(8) Immonen, M.; Zhang, R.; Press, M.; Tang, H.; Lei, V.; Wu, J.; Yan, H. J.; Zhu, L. X.; Serbay, M. End-to-end Optical 25Gb/s Link Demonstrator with Embedded Waveguides, 90° Out-of-Plane Connector and On-board Optical Transceivers. *42nd European Conference on Optical Communication (ECOC)*, 2016; pp 1−3.

(9) Shi, F.; Bamiedakis, N.; Vasilev, P. P.; Penty, R. V.; White, I. H.; Chu, D. Flexible Multimode Polymer Waveguide Arrays for Versatile High-Speed Short-Reach Communication Links. *J. Lightwave Technol.* **2018**, *36*, 2685−2693.

(10) Lei, K.-L.; Chow, C.-F.; Tsang, K.-C.; Lei, E. N. Y.; Roy, V. A. L.; Lam, M. H. W.; Lee, C. S.; Pun, E. Y. B.; Li, J. Long aliphatic chain coated rare-earth nanocrystal as polymer-based optical waveguide amplifiers. *J. Mater. Chem.* **2010**, *20*, 7526−7529.

(11) Zhai, X.; Liu, S.; Liu, X.; Wang, F.; Zhang, D.; Qin, G.; Qin, W. Sub-10 nm $BaYF_5$:Yb^{3+},Er^{3+} core−shell nanoparticles with intense 1.53 mm fluorescence for polymer-based waveguide amplifiers. *J. Mater. Chem. C* **2013**, *1*, 1525−1530.

(12) Yang, Z.; Wu, H.; Liao, J.; Li, W.; Song, Z.; Yang, Y.; Zhou, D.; Wang, R.; Qiu, J. Infrared to visible upconversion luminescence in Er^{3+}/Yb^{3+} co-doped CeO_2 inverse opal. *J. Mater. Sci. Eng. B* **2013**, *178*, 977−981.

(13) Zhai, X.; Li, J.; Liu, S.; Liu, X.; Zhao, D.; Wang, F.; Zhang, D.; Qin, G.; Qin, W. Enhancement of 1.53 μm emission band in $NaYF_4$:Er^{3+}, Yb^{3+},Ce^{3+} nanocrystals for polymer-based optical waveguide amplifiers. *Opt. Mater. Express* **2013**, *3*, 270−277.

(14) Wang, T.; Zhao, D.; Zhang, M.; Yin, J.; Song, W.; Jia, Z.; Wang, X.; Qin, G.; Qin, W.; Wang, F.; Zhang, D. Optical waveguide amplifiers based on $NaYF_4$: Er^{3+}, Yb^{3+} NPs-PMMA covalent-linking nanocomposites. *Opt. Mater. Express* **2015**, *5*, 469−476.

(15) Zhang, M.; Zhang, W.; Wang, F.; Zhao, D.; Qu, C.; Wang, X.; Yi, Y.; Cassan, E.; Zhang, D. High-gain polymer optical waveguide amplifiers based on core-shell $NaYF_4$/$NaLuF_4$: Yb^{3+}, Er^{3+} NPs-PMMA covalent linking nanocomposites. *Sci. Rep.* **2016**, *6*, 36729.

(16) Wang, Z.; Comyn, T. P.; Ghadiri, M.; Kale, G. M. Maltose and pectin assisted sol-gel production of $Ce_{0.8}Gd_{0.2}O_{1.9}$ solid electrolyte nanopowders for solid oxide fuel cells. *J. Mater. Chem.* **2011**, *21*, 16494−16499.

(17) Wang, Z.; Kale, G. M.; Ghadiri, M. Sol-gel production of $Ce_{0.8}Gd_{0.2}O_{1.9}$ nanopowders using Sucrose and Pectin as organic precursors. *J. Am. Ceram. Soc.* **2012**, *95*, 2863−2868.

(18) Wang, Z.; Kale, G. M.; Ghadiri, M. Synthesis and characterisation of $Ce_xGd_{1-x}O_{2-\delta}$ nanopowders employing an alginate mediated ion-exchange process. *Chem. Eng. J.* **2012**, *198−199*, 149−153.

(19) Florea, M.; Avram, D.; Cojocaru, B.; Tiseanu, I.; Parvulescu, V.; Tiseanu, C. Defect induced tunable near infrared emission of Er−CeO_2 by heterovalent co-dopants. *Phys. Chem. Chem. Phys.* **2016**, *18*, 18268−18277.

(20) Sani, E.; Toncelli, A.; Tonelli, M.; Lis, D. A.; Zharikov, E. V.; Subbotin, K. A.; Smirnov, V. A. Effect of Cerium on cooping in Er^{3+}, Ce^{3+}:$NaLa(MoO_4)_2$ crystals. *J. Appl. Phys.* **2005**, *97*, 123531.

(21) Shehata, N.; Meehan, K.; Hassounah, I.; Hudait, M.; Jain, N.; Clavel, M.; Elhelw, S.; Madi, N. Reduced erbium-doped ceria nanoparticles: one nano-host applicable for simultaneous optical down- and up-conversions. *Nanoscale Res. Lett.* **2014**, *9*, 231.

(22) Chiu, F.-C.; Lai, C.-M. Optical and electrical characterization of cerium oxide thin films. *J. Phys. D: Appl. Phys.* **2010**, *43*, 075104.
(23) Hass, G.; Ramsey, J. B.; Thun, R. Optical Properties and Structure of Cerium Dioxide Films. *J. Opt. Soc. Am.* **1958**, *48*, 324−327.
(24) Oh, T.-S.; Tokpanov, Y. S.; Hao, Y.; Jung, W.; Haile, S. M. Determination of optical and microstructural parameters of ceria films. *J. Appl. Phys.* **2012**, *112*, 103535.
(25) Porosnicu, I.; Avram, D.; Cojocaru, B.; Florea, M.; Tiseanu, C. Up-conversion luminescence of Er(Yb)-CeO_2: Status and new results. *J. Alloys Compd.* **2017**, *711*, 627−636.
(26) Yang, Z.; Wu, H.; Liao, J.; Li, W.; Song, Z.; Yang, Y.; Zhou, D.; Wang, R.; Qiu, J. Infrared to visible upconversion luminescence in Er^{3+}/Yb^{3+} co-doped CeO_2 inverse opal. *J. Mater. Sci. Eng. B* **2013**, *178*, 977−981.
(27) Guo, H.; Yang, X.; Xiao, T.; Zhang, W.; Lou, L.; Mugnier, J. Structure and optical of sol-gel derived Gd_2O_3 waveguide films. *Appl. Surf. Sci.* **2004**, *230*, 215−221.
(28) Dikmen, S.; Shuk, P.; Greenblatt, M.; Gocmez, H. Hydrothermal synthesis and properties of Ce_{1-x} $GdxO_2$-δ solid solutions. *Solid State Sci.* **2002**, *4*, 585−590.
(29) Dell'Agli, G.; Mascolo, G.; Mascolo, M. C.; Pagliuca, C. Weakly agglomerated nanocrystalline $(ZrO_2)_{0.9}(Yb2O_3)_{0.1}$ powders hydrothermally synthesized at low temperature. *Solid State Sci.* **2006**, *8*, 1046−1050.
(30) Yan, Z.; Wang, J.; Zou, R.; Liu, L.; Zhang, Z.; Wang, X. Hydrothermal Synthesis of CeO_2 Nanoparticles on Activated Carbon with Enhanced Desulfurization Activity. *Energy Fuels* **2012**, *26*, 5879−5886.
(31) Mokkelbost, T.; Kaus, I.; Grande, T.; Einarsrud, M.-A. Combustion Synthesis and Characterization of Nanocrystalline CeO_2-Based Powders. *Chem. Mater.* **2004**, *16*, 5489−5494.
(32) Laberty-Robert, C.; Long, J. W.; Lucas, E. M.; Pettigrew, K. A.; Stroud, R. M.; Doescher, M. S.; Rolison, D. R. Sol−Gel-Derived Ceria Nanoarchitectures: Synthesis, Characterization, and Electrical Properties. *Chem. Mater.* **2006**, *18*, 50−58.
(33) Rahayu, S.; Forrester, J. S.; Kale, G. M.; Ghadiri, M. Promising solid electrolyte material for an IT-SOFC: crystal structure of the cerium gadolinium holmium oxide $Ce_{0.8}Gd_{0.1}Ho_{0.1}O_{1.9}$ between 295 and 1023 K. *Acta Crystallogr.* **2018**, *74*, 236−239.
(34) Ghatrehsamani, S.; Town, G. E. Optical gain in polymer composite materials with P_2O_2: Er^{3+}/Yb^{3+}- codoped nanoparticles. *IEEE J. Quantum Electron.* **2017**, *53*, 7000705.
(35) Chen, F. R.; Zhao, X.; Sun, Y.; He, C.; Tan, M. C.; Tan, D. T. H. Low loss nanostructured polymers for chip-scale waveguide amplifiers. *Sci. Rep.* **2017**, *7*, 3366.
(36) Kumi-Barimah, E. ; Ziarko, M. W.; Bamiedakis, N.; White, I. H.; Penty, R. V.; Jose, G. Erbium-doped glass nanoparticle embedded polymer thin films using femtosecond pulsed laser deposition. *Opt. Mater. Express* **2018**, *8*, 1997−2007.
(37) Jeyanthi, C. E.; Siddheswaram, R.; Kumar, P.; Signh, J.; Hui, K. N.; Hui, K. S.; Rajaraja, K. Synthesis, characteristics and spectroscopic analysis of Er-doped ceria $(Ce_{0.9}Er_{0.1}O_{1.95})$ electrolyte for solid oxide fuel cells. *Ener. Environ. Focus* **2014**, 3, 196−201.
(38) Cui, J.; Hope, G. A. Raman and fluorescence spectroscopy of CeO_2, Er_2O_3, Nd_2O_3, Tm_2O_3,Yb_2O_3, La_2O_3, and Tb_4O_7. *J. Spectrosc.* **2015**, *2015*, 1−8.
(39) Albarkaty, K. S.; Kumi-Barimah, E.; Craig, C.; Hewak, D.; Jose, G.; Chandrappan, J. Erbium-doped chalcogenide glass thin film on silicon using femtosecond pulsed laser with different deposition temperatures. *Appl. Phys. A* **2019**, *125*, 1−8.
(40) Carteret, C.; Labrosse, A. Vibrational properties of polysiloxanes: from dimer to oligomers and polymers.1. Structural and vibrational properties of hexamethyldisiloxane $(CH_3)_3SiOSi(CH_3)_3$. *J. Raman Spectrosc.* **2010**, *41*, 996−1004.
(41) Jayes, L.; Hard, A. P.; Séné, C.; Parker, S. F.; Jayasooriya, U. A. Vibrational spectroscopy analysis of silicones: A Fourier Transforms-Raman and inelastic neutron scattering investigation. *Anal. Chem.* **2003**, *75*, 742−746.
(42) Steinkemper, H.; Fischer, S.; Hermle, M.; Goldschmidt, J. C. Stark level analysis of the spectral line shape of electronic transitions in rare earth ions embedded in host crystals. *New J. Phys.* **2013**, *15*, 053033.
(43) Inaba, T.; Tawara, T.; Omi, H.; Yamamoto, H.; Gotoh, H. Epitaxial growth and optical properties of Er-doped CeO_2on Si(111). *Opt. Mater. Express* **2018**, *8*, 2843−2849.
(44) Hu, Q.; Yang, F.; Fang, H.; Zhao, C. The preparation and electrical properties of La doped $Er_{0.2}Ce_{0.8}O_{1.9}$ based solid electrolyte. *Int. J. Electrochem. Sci.* **2017**, *12*, 7411−7425.
(45) Shan, X.; Tang, G.; Chen, X.; Peng, S.; Liu, W.; Qian, Q.; Chen, D.; Yang, Z. Silver nanoparticles enhanced near-infrared luminescence of Er^{3+}/Yb^{3+} co-doped multicomponent phosphate glasses. *J. Rare Earths* **2016**, *34*, 868−875.
(46) Wang, X.; Nie, Q.; Xu, T.; Dai, S.; Shen, X.; Liu, L. Optical spectroscopy and energy transfer of Er^{3+}/Ce^{3+} in B_2O_3 -doped bismuth−silicate glasses. *J. Opt. Soc. Amer. B* **2007**, *24*, 972−978.
(47) Yang, F.-j.; Huang, B.; Wu, L.-b.; Qi, Y.-w.; Peng, S.-x.; Li, J.; Zhou, Y.-X. Enhancement of fluorescence emission and signal gain at 1.53 μm in Er^{3+}/Ce^{3+} co-doped tellurite glass fiber. *Optoelectron. Lett.* **2015**, *11*, 361−365.
(48) Lu, H.; Gillin, W. P.; Hernández, I. Concentration dependence of the up- and down-conversion emission colours of Er^{3+}-doped Y_2O_3: a time-resolved spectroscopy analysis. *Phys. Chem. Chem. Phys.* **2014**, *16*, 20957−20963.
(49) Wang, X.; Nie, Q.; Xu, T.; Dai, S.; Shen, X.; Liu, L. Optical spectroscopy and energy transfer of Er^{3+}/Ce^{3+} in B_2O_3-doped bismuth−silicate glasses. *J. Opt. Soc. Am. B* **2007**, *24*, 972−978.
(50) Jiang, S.; Myers, M.; Peyghambarian, N. Er^{3+} doped phosphate glasses and lasers. *J. Non-Cryst. Solids* **1998**, *239*, 143−148.

https://dx.doi.org/10.1021/acsomega.0c00040
ACS Omega 2020, 5, 9224−9232